ARTICLE

Synergistic Promotion of Transition Metal Ion-exchange in TiO_2 Nanoarray-based Monolithic Catalysts for Selective Catalytic Reduction of NO_x with NH_3

Received 00th January 20xx,
Accepted 00th January 20xx

DOI: 10.1039/x0xx00000x

Xingxu Lu[a,b], Yanliu Dang[b], Meilin Li[c], Chunxiang Zhu[a,b], Fangyuan Liu[b], Wenxiang Tang[a,b], Junfei Weng[a,b], Mingyue Ruan[a], Steven L. Suib[b,c], Pu-Xian Gao[a,b,*]

TiO_2 supported catalysts have been widely studied for selective catalytic reduction (SCR) of NO_x, however the comprehensive understanding of the synergistic interactions in multi-component SCR catalysts is still lacking. Herein, transition metal elements (V, Cr, Mn, Fe, Co, Ni, Cu, La and Ce) were loaded onto TiO_2 nanoarrays *via* ion-exchange using the protonated titanate precursors. Amongst these catalysts, Mn-doped catalysts outperform the others with satisfactory NO conversion and N_2 selectivity. The Cu co-doping to the Mn-based catalysts promotes their low-temperature activity by improving reducibility, enhancing surface Mn^{4+} species and chemisorbed labile oxygen, and elevating adsorption capacity of NH_3 and NO_x species. While the Ce co-doping with Mn prohibits the surface adsorption and formation of NH_3 and NO_x derived species, it boosts the N_2 selectivity at high temperatures. By combining Cu and Ce as the doping elements into the Mn-based catalysts, both the low-temperature activity and the high temperature N_2 selectivity are enhanced, and the Langmuir-Hinshelwood reaction mechanism was proved to dominate in the trimetallic Cu-Ce-5Mn/TiO_2 catalysts due to the low energy barrier.

1. Introduction

With the rapid industrialization and urbanization, nitric oxides (NO_x, including NO and NO_2) emissions have become a major air pollutant and drawn increasing public attentions due to their serious environmental issues, including acid rain, photochemical smog, ozone depletion, and greenhouse effects.[1] Moreover, NO_x emissions can also accelerate the formation of secondary aerosol and fine particles such as PM 2.5, which further threatens human health and environment.[2, 3] Therefore, governments and researchers around the world have been devoting continuous efforts to fight against NO_x pollution.

Amongst various technologies, the selective catalytic reduction using NH_3 as the reducing agent (NH_3-SCR) to react selectively with NO_x to form N_2 and H_2O has been proven as the most effective way to reduce NO_x emission from both the stationary and mobile sources.[4-7] In the past decades, much progress has been made in the SCR catalysts, which can be categorized into three major groups, namely the noble metals, transition metal oxides, and transition metal ion exchanged zeolites. Particularly, the transition-metal oxides and their derivatives, especially the Mn,[8, 9] Ce[10, 11] and Cu[6, 12] based catalysts, received great attention for their earth-abundance, low-cost, environment-friendliness, high stability, and remarkable redox activity.[13] However, the synergistic interactions between the various elements in the multi-component catalysts require further elucidation.[8, 13-16]

Meanwhile, SCR catalysts are usually supported on other materials, such as Al_2O_3, TiO_2, carbon and ceramic monolith,[17] etc., to achieve an optimal SCR performance.[18] Among these support materials, TiO_2 is less acidic and offers excellent dispersion of active components and SO_2 resistance, therefore it has been widely used in NH_3-SCR catalysts.[13, 19-21] Moreover, layered protonated titanates (LPTs, $H_2Ti_2O_5 \cdot H_2O$) are the precursors of TiO_2 and were reported as the ideal support material due to its high surface area and abundant ion-exchangeable sites.[22-24] The theoretical cation exchange capacity (CEC) is 9.05 mmol/g for the monovalent ions of the layered di-titanate, outperforming other common ion exchangers with CECs in the range of 0.25-0.6 mmol/g, such as the layered clays, zeolites, and zirconium phosphate.[25] The high surface area and abundant ion-exchanging positions allow an atomic-scale distribution of metal cations, thus achieving a higher metal loading and dispersion.[24, 26, 27]

In practical applications, monolithic catalysts are widely applied in the abatement of air pollutions from various sources.[28, 29] Especially, the nanostructured array (nanoarray) based monolithic catalysts have been successfully developed and demonstrated for various catalytic reactions in the past decades, such as the automotive aftertreatment, CO_2 hydrogenation and VOCs abatement.[30-32] Compared with the conventional washcoat counterparts, the nanoarray catalysts show enhanced materials utilization efficiency, improved thermal stability and mechanical robustness , and tuneable catalytic performance. The LPT nanoarray-based monolithic catalysts were also demonstrated for the diesel oxidation catalysts (DOC).[26, 33] Therefore, it would be of

[a] *Department of Materials Science and Engineering, University of Connecticut, Storrs, CT 06269, USA*
[b] *Institute of Materials Science, University of Connecticut, Storrs, CT 06269, USA*
[c] *Department of Chemistry, University of Connecticut, Storrs, CT 06269, USA*
* Corresponding author: Email: puxian.gao@uconn.edu
† Footnotes relating to the title and/or authors should appear here.
Electronic Supplementary Information (ESI) available: [details of any supplementary information available should be included here]. See DOI: 10.1039/x0xx00000x

great value to investigate the LPT-based monolithic catalyst for NO_x abatement.

This work aims to employ the LPT-derived TiO_2 nanoarrays as the support to elucidate the synergistic interactions between different transition metal elements (V, Cr, Mn, Fe, Co, Ni, Cu, La and Ce) during the NH_3-SCR process. Monometallic catalysts were firstly evaluated for the NH_3-SCR activity and N_2 selectivity. Subsequently, the Mn-based catalysts were selected as base material and the other transition metal elements were introduced as secondary dopants to make the bimetallic catalysts to elucidate the synergistic interactions between these elements. Finally, trimetallic Cu-Ce-Mn/TiO_2 catalysts with different transition metal element loading amount and ratios were prepared and evaluated, and the synergistic effects of the different elements were systematically studied by various technologies.

2. Materials and Methods

2.1 Materials Preparation

The LPT nanoarrays were integrated onto the cordierite monoliths *via* a microwave-assisted hydrothermal method reported previously.[33] The transition metal elements were loaded onto the ion-exchangeable LPT nanoarrays through an wet-impregnation process, which was carried out at 80 °C for 12 h, and then the solution was evaporated at 80 °C until dry. Finally, the samples were calcined at 500°C for 2 hours, during which, the LPT nanoarrays transformed into anatase TiO_2, resulting the TiO_2 nanoarray supported transition metal catalysts (X/TNA). The detailed preparation procedures can be found in the Supporting Information (SI), and the catalysts composition are summarized in **Table S1**.

2.2 Catalyst Characterization

The X-ray diffraction (XRD) of the catalysts were conducted on a Bruker D2 X-ray diffractometer (Cu Kα, 30 kV, 10 mA). The morphology, composition and structure of the catalysts were characterized using a field-emission scanning electron microscope (SEM, ThermoFisher, TeneoLoVac) and a high-resolution scanning transmission electron microscope (STEM, ThermoFisher, Talos F200X S/TEM, 200 kV). The X-ray photoelectron spectroscopy (XPS) were performed on a Quantum 2000 Scanning ESCA Microprobe, using a monochromatic Al Kα X-ray source with the binding energy calibrated using the C 1s transition at 284.8 eV as an internal standard. The specific surface areas were measured by the Brunauer–Emmett–Teller (BET) method from the nitrogen adsorption–desorption isotherms measured at 77 K using a Micromeritics ASAP 2020 Automatic Chemisorption Analyzer.[34] Hydrogen temperature programmed reduction (H_2-TPR) was carried out in a ChemiSorb 2720 Pulse Chemisorption System equipped with a thermal conductivity detector (TCD) to study the reducibility of the catalysts. Temperature Programmed Desorption (TPD) were performed to study the adsorption and desorption properties towards NH_3 and NO_x species over the catalysts using a fixed-bed tube reactor connected to a Fourier transform infrared spectrometer (FTIR, ThermoFisher Nicolet 6700). The detailed description of the TPR and TPD measurements can be found in SI.

2.3 Catalytic Performance Evaluation

The catalytic performance evaluations were conducted using the same fixed-bed quartz reactor tube as the TPD tests. The feed gas was 500 ppm NO + 500 ppm NH_3 + 5 vol.% O_2 balanced with N_2 with a total flow rate of 300 sccm and a space velocity of 15,000 /h. The composition of exit gases including NO, NH_3, NO_2, and N_2O were continuously analyzed by an online FTIR. For catalytic activity data were collected at each designed temperature for 20 min to reach a steady state. All the samples were degreened in the reacting atmosphere at 500 °C for 4 hours before the tests. The NO conversion and N_2 selectivity were calculated by the following equations:

$$\text{NO conversion} = \frac{[\text{NO}]_{\text{in}} - [\text{NO}]_{\text{out}}}{[\text{NO}]_{\text{in}}} \times 100\%$$

$$\text{N}_2 \text{ selectivity} = \frac{[\text{NO}]_{\text{in}} - [\text{NO}]_{\text{out}} + [\text{NH}_3]_{\text{in}} - [\text{NH}_3]_{\text{out}} - [\text{NO}_2]_{\text{out}} - 2[\text{N}_2\text{O}]_{\text{out}}}{[\text{NO}]_{\text{in}} - [\text{NO}]_{\text{out}} + [\text{NH}_3]_{\text{in}} - [\text{NH}_3]_{\text{out}}} \times 100\%$$

The selected catalysts were also evaluated by the long-term stability and sulfur poisoning resistance tests, and the detailed procedures can be found in the SI.

2.4 *In situ* DRIFTS

In situ diffuse reflectance infrared Fourier transform spectroscopy (*in situ* DRIFTS) was conducted using a Nicolet iS50 FTIR (Thermal Fisher Scientific) equipped with a Harrick Praying Mantis unit. The samples were ground to powders and mounted in the IR cell, which was connected to a gas distribution manifold. Prior to each test, the catalysts were pre-treated at 500 °C in a flow of 10% O_2/N_2 for 30 min and cooled down to target temperature in N_2. Background spectra were recorded in a N_2 flow and automatically subtracted from the spectra. All spectra were recorded over accumulative 64 scans with a resolution of 4 cm^{-1} in the range of 4000–650 cm^{-1}. The feed contents of NO, NH_3, and O_2 in the gas mixture were 500 ppm, 500 ppm, and 5 vol.% (when used), respectively, with N_2 as balance with a flow rate of 100 sccm.

3. Results and Discussion

3.1 Catalytic Performance Tests

The catalytic performance of all the TiO_2 nanoarray (TNA) supported mono-, bi- and trimetallic catalysts were evaluated and summarized in **Fig. 1** and **Fig. S1-S4**. As displayed in **Fig. S1**, the V, Cr, Mn, Fe, Cu and Ce based monometallic catalysts exhibited SCR activity, while no obvious NO conversion was observed over the Co, Ni, and La impregnated samples. The negative NO conversions at high temperatures are due to the formation of NO *via* side reaction of $4NH_3 + 5O_2 = 4NO + 6H_2O$. Among the active samples, the Cr, Mn, Cu and Ce based catalysts showed higher NO conversions, however, the Cr/TNA exhibited low N_2 selectivity due to the formation of NO_2 and N_2O through side reactions at high temperatures (**Fig. S1b-d**). Particularly, the highest NO conversion of 61% was obtained over the Cu/TNA at 217 °C, but the N_2 selectivity decreases with increasing temperature due to the formation of NO and NO_2. Meanwhile, the Ce/TNA catalyst exhibited low activity at low temperatures, but the NO conversion outperformed the other samples at high temperatures with the N_2 selectivity close to 100% over the entire temperature range. Among these monometallic catalysts, Mn/TNA showed a satisfactory low-temperature activity and high temperature N_2

selectivity. Therefore, Mn/TNA was selected as a base catalyst and the other metal elements were doped to investigate the synergistic interactions between these elements on the NH_3-SCR.

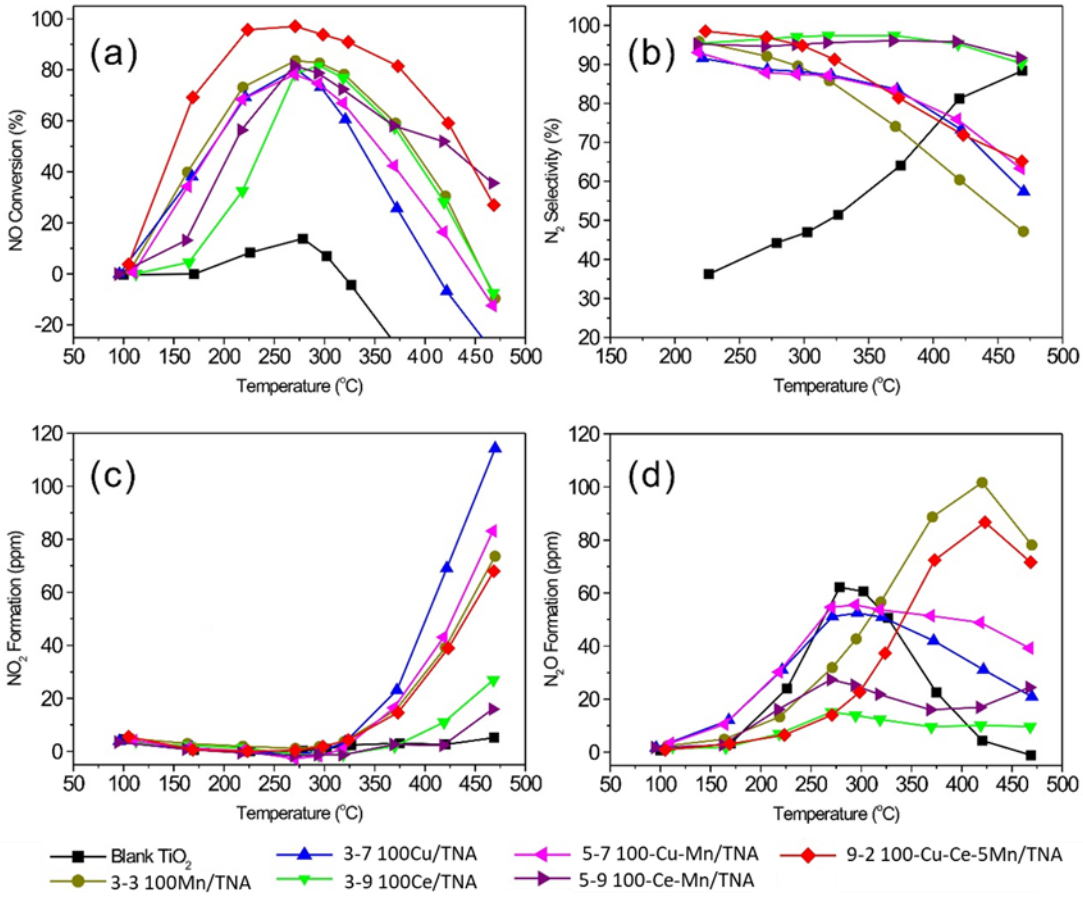

Fig. 1 Catalytic performance of the selected transition metal (i.e., Cu, Mn, and Ce) doped TiO_2 nanoarray based monolithic catalysts: (a) NO conversion, (b) N_2 selectivity, (c) NO_2 formation, and (d) N_2O formation. Feed gas: 500 ppm NO + 500 ppm NH_3 + 5 vol.% O_2 balanced with N_2 and space velocity of 15,000 /h.

The effects of the secondary dopant elements on the Mn/TNA catalysts were evaluated by keeping the total loading metal amount at 50 g/ft^3. As shown in **Fig. S2**, the Cr, Cu, and Ce doped bimetallic catalysts show promoted NO conversion at low temperatures (**Fig. S2a**). However, like the results over the mono-metallic catalysts shown in **Fig. S1**, the high-temperature N_2 selectivity of the bi-metallic Cr-Mn/TNA and Cu-Mn/TNA deteriorates due to the formation of NO_2 and N_2O through side reactions. As for the Ce-doped catalyst, both the high-temperature NO conversion and N_2 selectivity were promoted, but the low temperature reactivity is not as good as Cu-Mn/TNA. Thus, based on the results over the mono- and bimetallic catalysts and considering the low toxicity of the dopant elements, Cu, Ce, and Mn were selected and three groups of trimetallic Cu-Ce-Mn/TNA catalysts with different loading amounts and atomic ratios were prepared for further evaluation. As displayed in **Fig. S3**, the 100Cu-Ce-5Mn/TNA sample with an atomic ratio of Cu/Ce/Mn=1/1/5 and a total metal loading of 100 g/ft^3 exhibited the highest NO conversion of 97% at 270 °C over a wide temperature range. Therefore, six representative catalysts with the total metal loading of 100 g/ft^3 were selected for further study on the synergy of different elements for NH_3-SCR. As displayed in **Fig. 1**, the Cu-Ce-5Mn/TNA catalyst outperforms the mono- and bimetallic samples, which demonstrates the synergistic interactions among the Cu, Ce, and Mn elements can greatly promote the NH_3-SCR performance and maintain high N_2 selectivity over a wide temperature window.

Furthermore, the Cu-Ce-5Mn/TNA catalysts were also tested for stability and sulfur poisoning resistance, respectively. As shown in **Fig. S4a**, after being exposed to the reaction atmosphere at 220 and 315 °C for 40-50 hours, no obvious decrease in the NO conversion or the N_2 selectivity were observed over the Cu-Ce-5Mn/TNA catalyst. Specifically, the catalyst exhibited higher NO conversion (> 95%) and N_2 selectivity (> 97%) at 220 °C than at 315 °C, which is due to the enhanced side reactions at higher temperatures. On the other hand, sulfur-containing compounds exist in most vehicle fuels and lubricants, which forms SO_2 and deactivate the catalysts.[19, 35] In this work, the exposure to SO_2 resulted in decreases in NO conversion from 97 to 79% and 95 to 91% at 220 and 270 °C, respectively. However, the sulfur poisoning inhibits more on the side reactions than on the main NO abatement reaction, resulting in a higher NO conversion and N_2 selectivity than the pristine sample at temperatures. Based on the experimental data obtained under the laboratory conditions in the present work, more realistic exhaust tests will be conducted over the samples in our subsequent studies by considering the presence of water content, hydrocarbons, and other components.

3.2 Structural, Compositional and Porosity Properties

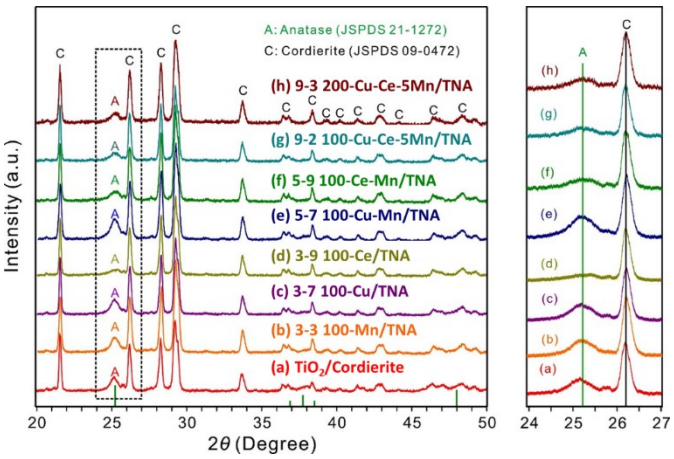

Fig. 2 XRD patterns: (a) TiO_2; (b) 100Mn/TNA; (c) 100Cu/TNA; (d) 100Ce/TNA; (e) 100-Cu-Mn/TNA; (f) 100-Ce-Mn/TNA; (g) 100-Cu-Ce-5Mn/TNA; (h) 200-Cu-Ce-5Mn/TNA. Patterns in the box are enlarged on the right.

The catalytic performance of the SCR catalysts is directly related to the structural and compositional properties. The XRD patterns of the TiO_2 nanoarray supported catalysts are displayed in **Fig. 2**, in which, only the diffraction peaks of anatase TiO_2 (JSPDS 21-1272) and cordierite (JSPDS 09-0472) are detectable, and the Raman spectra in **Fig. S5** also exhibit the bands of anatase TiO_2. The absence of the peaks of the metal oxides of Cu, Ce, and Mn suggests the complete intercalation of the Cu, Ce, and Mn atoms into the anatase lattice, which will be further evidenced by the TEM and elemental mapping results in **Fig. 3**. Furthermore, for all the samples without Ce doping, i.e., the blank TiO_2, Mn/TNA, Cu/TNA and Cu-Mn/TNA, a sharp peak at 25.28° from the anatase (101) planes is observable (**Figs. 2a**, **b**, **c**, and **e**). However, this peak becomes flattened upon Ce addition in the Ce/TNA, Ce-Mn/TNA, and Cu-Ce/TNA (**Figs. 2d**, **f**, **g**, and **h**). The bright field (BF), high resolution TEM (HRTEM) and selected area electron diffraction (SAED) patterns of the Ce/TNA in **Fig. S7** exhibits distinctive diffraction rings of anatase TiO_2 with no phase segregation. Therefore, the flattened peaks but distinctive diffraction rings suggest that Ce-doping can reduce the crystal sizes of the anatase crystallites, as is further supported by the specific surface area results.

The SEM, BF, HRTEM, high angle annular dark field (HAADF) images, and elemental mapping of the LPT nanoarray rooted monolith and Cu-Ce-5Mn/TNA catalysts are presented in **Fig. 3**. As shown in **Fig. 3a-c**, LPT nanoarrays were uniformly integrated onto the channel surfaces of the cordierite monolith. Upon the ion-exchange with transition metal elements, secondary nanoflakes were formed on the nanoarrays, resulting in a 3D nanostructured framework (**Fig. 3d**, **e** and **k**). The SAED patterns (**Fig. 3j**) exhibit the diffraction rings of anatase TiO_2 with no diffraction patterns of the oxides of Mn, Cu, and Ce, which agrees with the XRD patterns in **Fig. 2**. The HRTEM of the nanoflakes (**Fig. 3f~i**) reveal the lattice of anatase (101) planes. The EDX mapping reveals the uniform distribution of Mn, Cu, and Ce

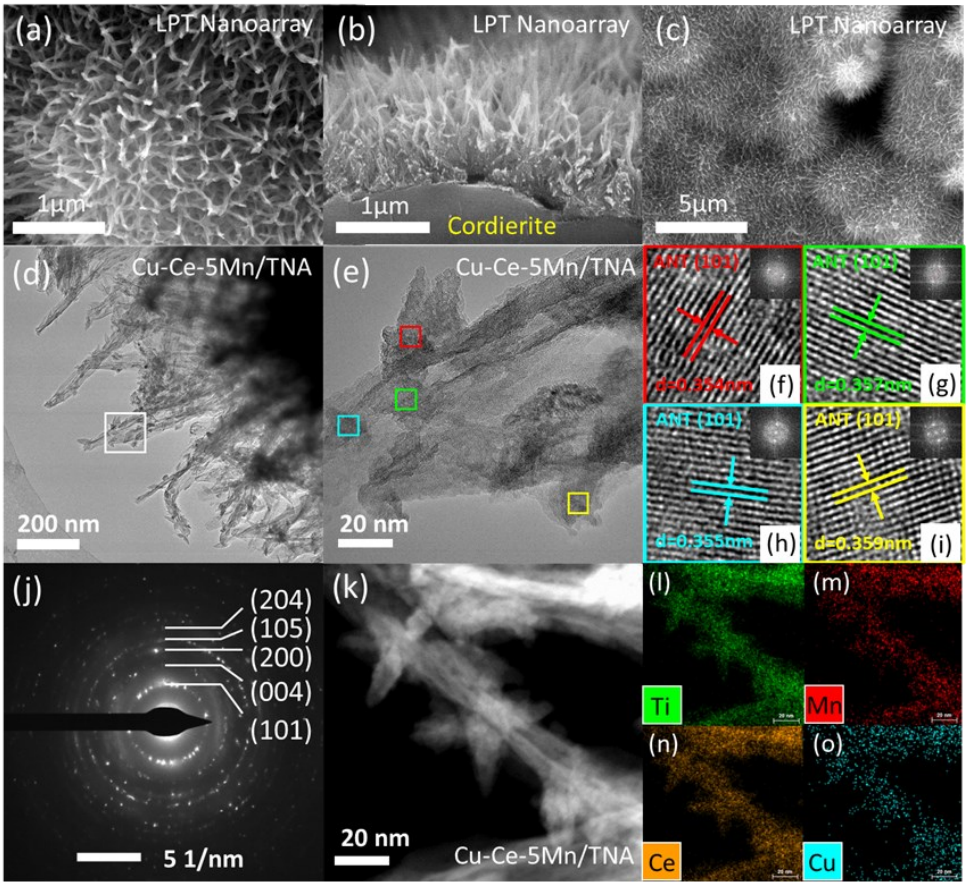

Fig. 3 SEM images of the LPT nanoarray-rooted monolith: the high-magnification (a) top view, (b) cross-section view, and low-magnification (c) top view. The BF (d-e) and HRTEM (f-i) images of the Cu-Ce-5Mn/TNA catalyst with the lattice indexed by anatase (101) plans. (j) The SAED patterns indexed by anatase TiO_2. (k) The HAADF image of the Cu-Ce-5Mn/TNA catalysts and (l)~(o) the EDX mapping showing the elemental distribution of Ti, Mn, Ce and Cu, respectively.

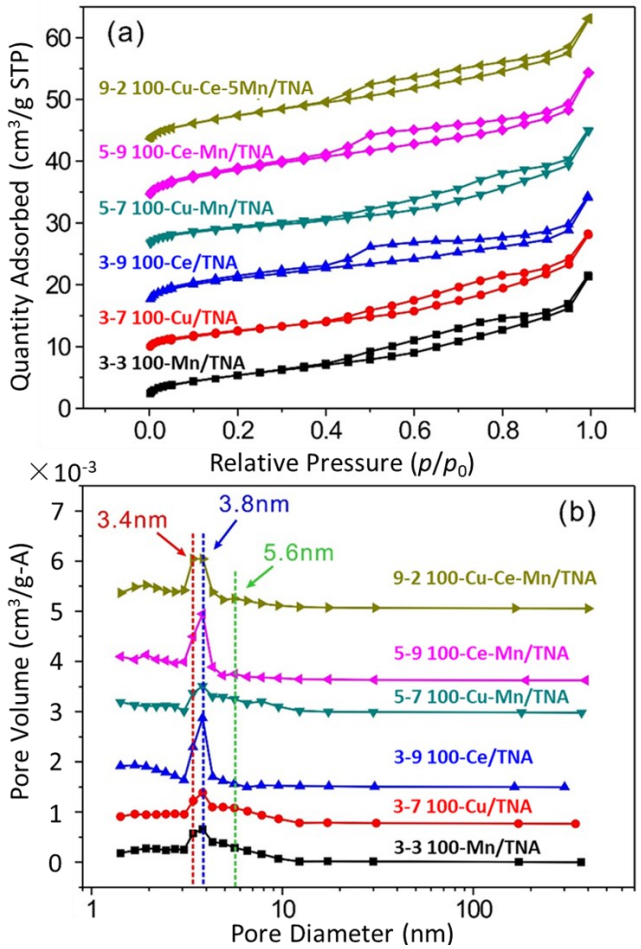

Fig. 4 (a) Nitrogen adsorption-desorption isotherms and (b) the BJH pore-size distribution of the selected catalysts.

atoms in both the primary nanorods and secondary nanoflakes (**Fig. 3m**, **n** and **o**), demonstrating that the dopant elements are intercalated into the TiO_2 lattice rather than attached on the surface of the nanorods. Interestingly, Ti atoms are also uniformly distributed in both the primary nanorods and secondary nanoflakes (**Fig. 3l**). Considering the LPT is the only Ti source, the distribution of Ti atoms on the secondary nanoflakes suggests a leaching-recrystallization process during ion-exchange when the Ti atoms were leached from the LPT nanorods by the transition metal nitrate solution at first, and then recrystallized to form the anatase nanoflakes on the primary LPT nanorods. Such leaching-recrystallization process was also observed during the synthesis of Ceria-based nanoflake arrays in our previous work.[28] The secondary nanoflake structures helps to increase the surface area and modify the properties of the catalysts, resulting in a better dispersion of the active sites and improved overall catalytic performance. The HRTEM and elemental mapping reveals the complete intercalation of the transition metal atoms into the anatase lattice with no phase segregation, which explains the absence of the characteristic peaks of the metal oxides in the XRD patterns in **Fig. 2**.

The BET isotherms and BJH pore-size distributions are summarized in **Fig. 4**. The N_2 adsorption-desorption isotherms of the transition metal doped catalysts show a type IV feature with a type H3 hysteresis loop, indicating the mesoporous structure with slit shaped pores formed by agglomerates of particles with non-uniform size and shape.[36] The Ce-doped samples show higher specific surface area due to the decreased the crystal sizes of the anatase nanocrystallites upon Ce addition, which agrees with the broadened XRD peaks of anatase phases in the Ce-doped samples in **Fig. 2**. The pore size distributions of the samples exhibit a range of 3.4~5.6 nm, suggesting the materials are mesoporous to facilitate the heterogeneous catalytic processes.[37]

3.3 Catalyst Reducibility and Surface Oxidation State

The H_2-TPR profiles of blank TiO_2 nanoarrays, mono-, bi- and tri-metallic catalysts are presented in **Fig. S8**, and the total H_2 consumptions are quantified in **Table 1**. The monometallic Mn/TNA catalyst (**Fig. S8b**) exhibits a broad reduction peak, which can be split into three peaks at 394, 451 and 519 °C corresponding to the reductions of Mn^{4+} to Mn^{3+}, Mn^{3+} to $Mn^{2.67+}$ and $Mn^{2.67+}$ to Mn^{2+}, respectively.[14, 38] Upon the introduction of Cu, the reduction peaks of the bi-metallic 100Cu-Mn/TNA catalyst (**Fig. S8e**) are significantly enhanced and shift to the lower temperatures, with a higher H_2 consumption of 3,504 μmole/g than the monometallic Mn/TNA catalyst (2,024 μmole/g). As is known, a higher H_2 consumption amount indicates a higher reducibility of a catalysts, and a lower peak H_2 reducing temperature suggests that the catalyst is easier to be reduced at low temperatures. Therefore, the H_2-TPR analysis help to partially explain the higher SCR reactivity of the Cu-doped samples at low temperatures, that the addition of Cu into the Mn-based catalysts helps to improve the reducibility of the catalysts, which contributes to the improved low-temperature SCR reactivity for NO reduction. On the other hand, the addition of Ce to the Mn/TNA catalyst results in a flattened H_2 reduction profile with a decreased H_2 consumption of 1,322 μmole/g (**Fig. S8f**), indicating that Ce as a dopant compromises the reducibility of the Mn/TNA catalysts, which is in accordance with the diminished low-temperature activity of the Ce-Mn/TNA catalysts. Finally, the H_2-TPR profile of the trimetallic Cu-Ce-5Mn/TNA catalyst combines the features of the mono- and bimetallic catalysts, and four distinctive peaks are identified in **Fig. S8g**. Compared to Cu-Mn/TNA, the reduction temperatures of the Cu-Ce-5Mn/TNA catalysts increases, and the total H_2 consumption of the Cu-Ce-5Mn/TNA catalyst (2,123 μmole/g) is also lower than that of the Cu-Mn/TNA (3,504 μmole/g), which is due to the introduction of Ce element. The detailed discussion and identification of the H_2 reduction peaks for each sample can be found in SI.

The XPS of the Mn $2p_{3/2}$ and O 1s of the selected catalysts are deconvoluted in **Fig. 5** and the oxidation states and surface species in the catalysts are summarized and quantified in **Table 1**. As shown in **Fig. 5a-d**, the asymmetric peaks of Mn $2p_{3/2}$ spectra are split into three peaks centred at 640.7, 642.1 and 644.2 eV corresponding to Mn^{3+}, Mn^{4+} and Mn nitrates, respectively.[13, 39, 40] The Mn^{4+} is dominant for the low-temperature de-NO_x performance by facilitating the oxidation of NO to NO_2,[1, 8, 41] making the Mn^{4+}/Mn^{3+} ratio an indicator of SCR activity of the catalysts. For the monometallic Mn/TNA catalyst, the Mn^{4+}/Mn^{3+} =1.31, while the introduction of Cu and Ce change Mn^{4+}/Mn^{3+} ratios to 1.53 and 1.05, respectively. The increased Mn^{4+}/Mn^{3+} ratio in the Cu-Mn/TNA catalyst agrees with the H_2-TPR profile of the Cu-Mn/TNA catalyst with the enhanced reduction peak of Mn^{4+} to Mn^{3+}, which also helps to explain the better low-temperature activity of the Cu-Mn/TNA catalyst. The introduction of Ce, on the other hand, results in a decreased Mn^{4+}/Mn^{3+} ratio to 1.05, implying that the Ce doping can bring about the partial reduction of the Mn^{4+} to Mn^{3+}.[42] When both Cu and Ce are introduced, there is also

a significant increase of the Mn^{4+}/Mn^{3+} ratio from 1.31 to 1.69, which lends supports to the excellent overall performance of the trimetallic Cu-Ce-5Mn/TNA catalyst.

Table 1 Specific surface area, porosity, reduction temperatures, H_2 consumption and surface species of the selected catalysts.

Catalyst	S_{BET} (m^2/g)	Pore dia. (nm)	Reduction Temperature (°C)				H_2-TPR[a] (μmole/g)	NH_3-TPD[b]	[L]/[B][c]	Mn^{4+}/Mn^{3+}	O^{α}/O^{β}
			T_1	T_2	T_3	T_4					
Mn/TNA	19	3.83	394	451	519	--	2024	1.00	1.79	1.31	1.04
Cu/TNA	17	3.82	189	350	--	--	1792	--		--	--
Ce/TNA	22	3.83	291	363	495	--	1305	--		--	--
Cu-Mn/TNA	15	3.82	191	230	290	380	3504	1.11	1.88	1.53	0.98
Ce-Mn/TNA	25	3.83	284	368	484	664	1322	0.75	1.46	1.05	0.75
Cu-Ce-5Mn/TNA	24	3.83	206	293	335	372	2123	1.04	1.89	1.69	2.15

[a]: The H_2 consumption was calculated from the calibration experiments using Copper (II) oxide tested under the same conditions.
[b]: The amount of NH3-TPD was normalized according to the peak area of the Mn/TNA catalyst.
[c]: The ratio of the amount of Lewis acid sites [L] over the Brønsted acid sites [B] based on the deconvoluted peak area in the NH_3-TPD profiles.

The O 1s XPS spectra of the selected catalysts are deconvoluted into three peaks in **Fig. 5e-h**: lattice oxygen (529.5–530.2 eV, O^{β}), surface labile oxygen (530.1–530.8 eV, O^{α}) and adsorbed molecular water above 532 eV (O^{γ}).[15, 41, 43-45] The lattice oxygen O^{β} originates from Ti–O in the TiO_2 crystal, and the surface labile oxygen O^{α} result from the Ti–OH over the catalyst surface.[15, 46] The surface labile oxygen O^{α} is more active due to its higher mobility and illustrates a key role in oxidation reactions.[47, 48] Therefore, a high O^{α}/O^{β} ratio is beneficial for the NO oxidation to NO_2 in the SCR of NO_x reaction.[15, 47] As summarized in **Table 1**, the Mn/TNA, Cu-Mn/TNA and Ce-Mn/TNA catalysts exhibit approximate O^{α}/O^{β} ratio of 0.75~1.04. However, when both Cu and Ce are added, the O^{α}/O^{β} ratio significantly increases to 2.15, suggesting that the simultaneous introduction of Cu and Ce helps to increase the surface chemisorbed labile oxygen (O^{α}) and promote the oxidation of NO to NO_2 during the NH_3-SCR process.

3.4 Surface Adsorption and Desorption

The surface adsorption and desorption properties for the NH_3 and NO_x species over the selected catalysts were s by NH_3- and NO-TPD and displayed in **Fig. S9-S10** and **Fig. 6**. All the catalysts exhibit asymmetric NH_3 desorption peaks with a maximum centred at 130~150 °C and a shoulder at 195~233 °C (**Fig. S9**), which can be assigned to the NH^{4+} ions and the NH_3 molecules coordinated to the Brønsted and Lewis acid sites, respectively, considering the higher thermal stability of the Lewis acid sites.[49-53] Therefore, the ratios of the Lewis to Brønsted acid sites can be quantified based on the deconvoluted peak areas. As compared in **Fig. 6a**, the addition of Cu increases both the NH_3 adsorption and the ratio of the Lewis acid sites of the Mn-based catalysts, while the addition of Ce prohibits the NH_3 adsorption and Lewis's acid sites. According to the literature, the Lewis acid sites are more active than Brønsted acid sites in activating the NO molecules during NH_3-SCR.[49, 54] Therefore, the enhanced surface Lewis acid sites and NH_3 adsorption capacity facilitates the higher low-temperature activity of the Cu-doped catalysts.

The NO-TPD profiles (**Fig. S10**) generally exhibit two NO desorption peaks at 110 and 230 °C, which can be assigned to the physically and chemically adsorbed NO, respectively. Meanwhile, two NO_2 desorption peaks can be found in the approximate temperatures, indicating the oxidation of NO by the surface adsorbed oxygen. Moreover, there are slight amounts of N_2O released from some samples during the NO-TPD process. Both the Mn/TNA and Cu/TNA catalysts exhibit the desorption of NO, NO_2, and N_2O during the TPD process, however, Ce/TNA shows no desorption of NO_x at all. When Cu and Ce are introduced, the Cu-Mn/TNA show enhanced NO_x desorption with significant amount of NO_2, while the Ce-Mn/TNA shows no desorption of NO and NO_2 at 110 °C and no N_2O desorption in the whole temperature range. For the trimetallic Cu-Ce-5Mn/TNA catalysts, moderate amounts of NO, NO_2, and N_2O can be observed during the TPD process. The varied NO_x desorption behaviours of the catalysts reveal the different effects of these elements in the multi-component catalysts. Generally, the addition of Cu enhances the NO adsorption, and the strong desorption of NO_2 from the Cu-doped samples indicate the formation NO_2 in the presence of Cu, which explains the active low-temperature redox properties of the Cu

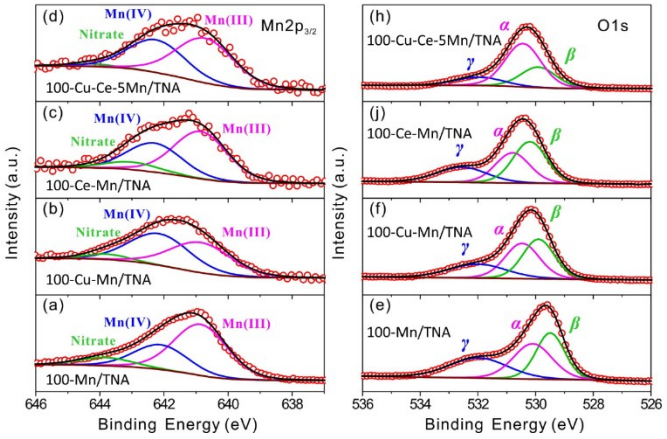

Fig. 5 Deconvoluted (a-d) Mn $2p_{3/2}$ and (e-h) O 1s XPS of the selected catalysts.

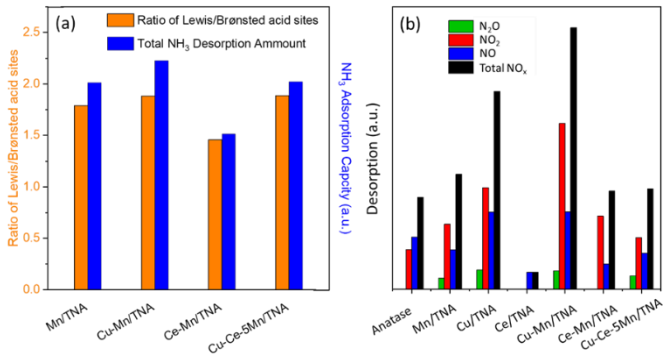

Fig. 6 (a) Quantified NH_3 adsorption capacity and ratio of the Lewis to Brønsted acid sites over the selected catalysts during the NH_3-TPD tests. (b) Quantified desorption of different NO_x species on selected catalysts during the NO-TPD tests.

species. The introduction of Ce, however, depresses the NO_x adsorption, resulting in the low reactivity of the Ce-based catalysts at low temperatures. Particularly, the addition of Ce preferably depresses the physically adsorbed NO and the formation of N_2O over the Ce-Mn/TNA catalyst, indicating the change in reaction routes and mechanisms. It should be noted that the desorbed NO_2 was formed through the oxidation of the adsorbed NO by the surface oxygen species identified by the O1s XPS spectra in **Fig. 5**.

3.5 Reaction Mechanism Study

The FTIR spectra of the surface adsorbed species derived from the NH_3 adsorption and co-adsorption of NO and O_2 over the selected catalysts at 150 °C are displayed and quantified in **Fig. 7**. As presented in **Fig. 7a** and **c**, the NH_3 adsorption over Mn/TNA resulted in the IR bands of the NH_3 coordinated on Lewis acid sites (1608, 1143 and 1043 cm^{-1}) [41, 55] and NH_4^+ bound to Brønsted acid sites (1444 cm^{-1}),[41, 56] which are denoted as NH_3(L) and NH^{4+}(B) in this work, respectively. The bands around 1542,[57] 1359,[58] and 1240 cm^{-1} [53] were attributed to the ammonia oxidation intermediates (M), free nitrate ions (N0), and the monodentate nitrates (N1), respectively. When doped with secondary elements, the addition of Ce prohibits the adsorption of Lewis acid sites NH_3 (L) and the NH_3 oxidation intermediates (M), but significantly enhances the NH_4^+ adsorption on Brønsted acid sites (B). The introduction of Cu, on the other hand, can significantly increase the Lewis acid sites NH_3 (L) and the ammonia oxidation intermediates (M) on the surface of the catalysts. The Lewis acid sites are produced by the coordinately unsaturated cationic sites, which are ready electron accepters and easy to activate NO molecules directly due to the one electron bond of the electronic structure.[54] Meanwhile, the Lewis acid sites could also activate the oxygen by electrostatic polarization, attacked by gas phase NO to form NO_2.[59] Therefore, the more surface Lewis acid sites, the more adsorption and activation sites for NO, which are crucial to promote the generation of adsorbed NO_2 and nitrate species over the catalyst surface. This also lend support to the enhanced adsorption capacity of NO_x species and low-temperature reactivity of the Cu-doped catalysts. The trimetallic Cu-Ce-5Mn/TNA catalyst showed an overall enhancement in the surface adsorbed species. Particularly, the peak intensity

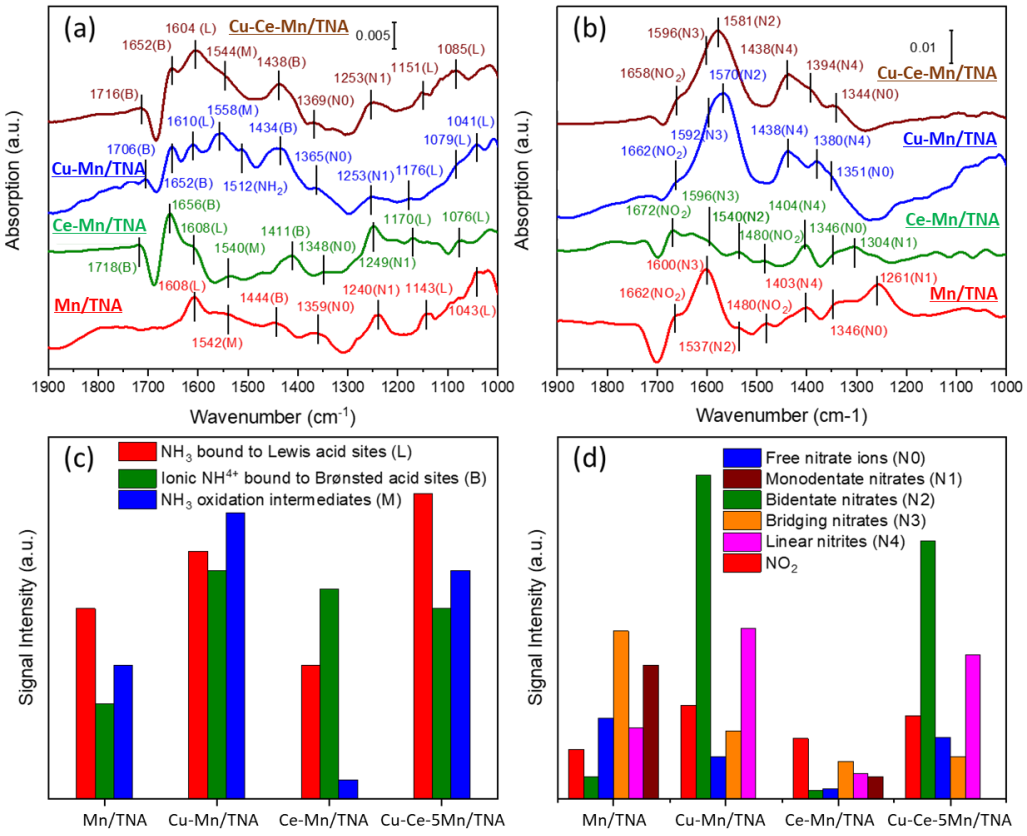

Fig. 7 FTIR spectra of (a) NH_3 adsorption and (b) NO + O_2 co-adsorption at 150 °C over the selected catalysts. Calculated quantities of various adsorbents (c) Lewis acid sites (L), Brønsted acid sites (B) and NH_3 oxidation intermediates (M) from NH_3 adsorption and (d) NO_x species derived from NO + O_2 co-adsorption.

associated to the NH_3 coordinated on Lewis's acid sites (L) are much higher than the monometallic and bimetallic catalysts, revealing that the synergy of Cu, Ce and Mn elements increase the quantity and percentage of Lewis acid sites on the catalyst surface.

Upon the co-adsorption of NO and O_2 (**Fig. 7b** and **d**), the monometallic Mn/TNA catalyst exhibits the adsorption of NO and O_2 with the IR bands 1662 and 1480 cm^{-1}, which correspond to the asymmetric stretching of coordinated NO_2 formed by NO oxidation and the M-NO_2 (M = Mn or Ti) nitro compounds, respectively.[49, 60] Other detected IR bands include the free nitrate ions (N0) at 1346 cm^{-1},[58] monodentate nitrates (N1) at 1261 cm^{-1},[41, 53] bidentate nitrate (N2) at 1537 cm^{-1},[41] bridging nitrates (N3) at 1600 cm^{-1},[49] and linear nitrite (N4) at 1403 cm^{-1}.[61] When the secondary dopant elements were introduced, the doping of Cu enhances the adsorption of NO_x as well as the formation of NO_2, bidentate nitrate (N2) and linear nitrite (N4) over the Mn-based catalysts, while the addition of Ce prohibited the adsorption of the NO_x species and the formation of intermediate compounds at 150 °C. Particularly, the adsorbed NO_2 originates not only from the gaseous NO_2 by the reaction between NO and O_2, but also from the *in situ* reaction between NO and the chemisorbed oxygen (O^{α}) on the catalyst surface.[49] The high O^{α}/O^{β} ratio over the Cu-doped catalysts facilitate the oxidation of NO to form NO_2 and boost the low temperature activity. According to the literature,[49] the presence of the adsorbed NO_2 on the selected samples favour the low temperature activity by "fast SCR". These observations can help to explain the higher catalytic activity of the Cu-doped catalysts than the Ce-doped counterparts in the low temperature range.

Time-resolved DRIFTS can help to directly clarify the reactive intermediates and possible reaction mechanism during the NH_3-SCR. The *in situ* DRIFTS of the surface reactions over the selected catalysts at 150 °C are summarized in **Fig. S11-S12** and **Fig. 8**. As presented in **Fig. 8a** and **b**, when NH_3 was firstly introduced, the surfaces of the trimetallic Cu-Ce-5Mn/TNA catalyst were quickly covered by the NH_3-derived species, which have been identified in **Fig. 7a**. After NO and O_2 were introduced, the NH_3 oxidation intermediates (M) were quickly consumed in 10 min, which suggests the existence of the NH_3-SCR root through the NH_3 oxidation intermediates (M). Meanwhile, the IR band at 1604 cm^{-1} also gradually shifts to 1581 cm^{-1} due to the consumption of the Lewis acid site coordinated NH_3 (L) and the formation of the bidentate nitrate (N2). The Brønsted acid site bounded NH_4^+ (B) were replaced by the NO_2 formed by NO oxidation and the accumulation of the linear nitrite (N4), resulting in the IR bands at 1658 and 1438 cm^{-1},[61] respectively. The IR band of the monodentate nitrates (N1) at 1253 cm^{-1} barely changed, revealing the low activity of this intermediate. The reaction between the pre-adsorbed NH_3-derived species and the gas phase NO suggests the presence of an Eley-Rideal (E-R) mechanism.

When the reactant was introduced in a reverse order, the *in situ* FTIR spectra of the surface reactions between NH_3 and the pre-adsorbed NO_x species at 150 °C over the Cu-Ce-5Mn/TNA catalyst are summarized in **Fig. 8c** and **d**. On the one hand, the absorbed NO_2 and bidentate nitrate (N2) were quickly consumed and replaced by the IR band of the NH_4^+ bound to Brønsted acid sites (B) at 1652 cm^{-1} [41, 56]. On the other hand, the IR band at 1581 cm^{-1} also quickly shifted to

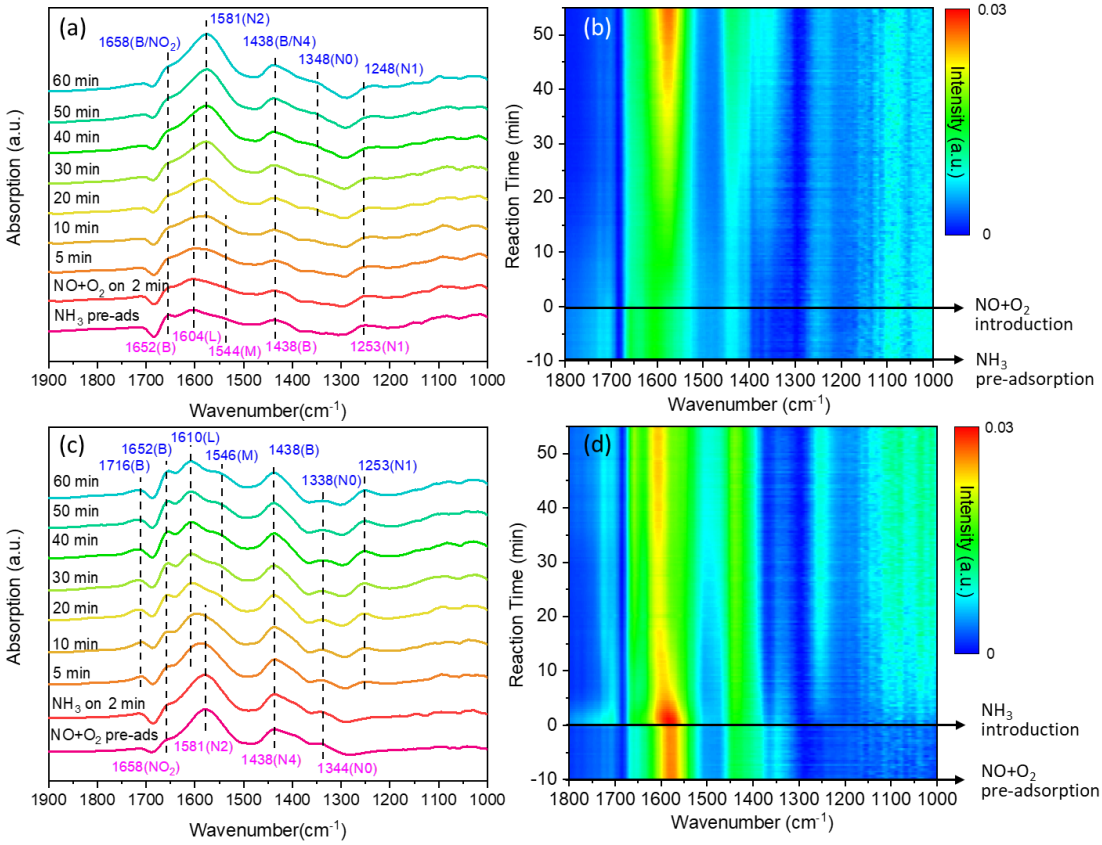

Fig. 8 *In situ* DRIFTS of (a, b) NO + O_2 reacted with pre-adsorbed NH_3 and (c, d) NH_3 reacted with pre-adsorbed NO + O_2 at 150 °C over the trimetallic Cu-Ce-5Mn/TNA catalyst. Conditions: [NO] = [NH_3] = 500 ppm, [O_2] = 5 vol.% (when used) and N_2.

1610 cm^{-1} with the consumption of the bidentate nitrate (N2) and adsorption of the NH_3 coordinated on Lewis acid sites (L). The linear nitrite (N4) was replaced by the NH_4^+ bound to Brønsted acid sites (B) at 1438 cm^{-1} [41, 56]. The changes of the spectra over Cu-Ce-5Mn/TNA illustrated the active surface reaction between NH_3 and pre-adsorbed NO_x species, which agrees with the Langmuir-Hinshelwood (L-H) mechanism of NH_3-SCR reaction[49]. Furthermore, it took ~10 min to consume the pre-adsorbed NO_x species by the introduced NH_3 (**Fig. 8c**), while it was not until ~40 min that the pre-adsorbed NH_3 on the Lewis acid sites (L) were consumed in **Fig. 8a**. The slow reaction between the NO and pre-adsorbed NH_3 suggests that the L-H mechanism is the dominant reaction pathway for the generation of N_2 over Cu-Ce-5Mn/TNA catalysts. This phenomenon agrees with previous reports about Ce-containing catalysts[62-64], attributing to the higher energy barrier of the first step of the E-R mechanism compared with that of L-H mechanism, which has been further confirmed by density functional theory calculation[65]. The detailed discussion on the evolution of the *in situ* DRIFTS over the mono- and bi-metallic catalysts can be found in the SI.

Conclusions

In summary, a series of TiO_2 nanoarray (TNA) supported transition metal catalysts were prepared and evaluated for NH_3-SCR. Based on the catalytic performance, Cu, Ce, and Mn were selected and the synergistic effects of these elements were studied over the mono-, bi- and trimetallic catalysts. The Mn/TNA catalysts exhibit a satisfactory low temperature SCR activity and high-temperature N_2 selectivity. The addition of Cu promotes the low-temperature activity by enhancing the catalyst reducibility, the ratio of Mn^{4+} and surface labile oxygen (O^{α}), and the activation of the Lewis acid site coordinated NH_3 (L) and the NO_x species. However, the N_2 selectivity decreased at high temperatures due to the formation of NO_2 and N_2O. The doping of Ce prohibits the adsorption and activation of the NH_3 and NO_x species but maintain a high N_2-selectivity at the elevated temperatures. Due to the synergistic interactions between the dopant elements, the L-H reaction mechanism dominates the NH_3-SCR process over the Cu-Ce-5Mn/TNA catalyst due to the rapid reaction between the adsorbed NH_3 and NO_x species. The addition of Cu also promotes the "fast SCR" through the formation of NO_2 from the adsorbed NO on the catalyst surfaces.

Author Contributions

Xingxu Lu: Data curation; Formal analysis; Investigation; Methodology; Software; Validation; Visualization; Writing - original draft. **Yanliu Dang**: Investigation. **Meilin Li**: Investigation. **Chunxiang Zhu**: Methodology. **Fangyuan Liu**: Investigation. **Wenxiang Tang**: Supervision. **Junfei Weng**: Investigation. **Mingyue Ruan**: Investigation. **Steven L. Suib**: Resources, Supervision. **Pu-Xian Gao**: Funding acquisition, Project administration, Resources, Supervision, Validation, Writing - review & editing.

Conflicts of interest

There are no conflicts to declare.

Acknowledgements

The authors are grateful for the financial support from the US Department of Energy (Award Nos. DE-SC0018890 and DE-EE0008423), the US National Science Foundation (Award No. IIP 1919231), and the University of Connecticut IMMP and CARIC programs. The SEM and TEM studies were performed using the facilities in the UConn/ThermoFisher Scientific Center for Advanced Microscopy and Materials Analysis (CAMMA).

References

1. C. Liu, J.-W. Shi, C. Gao and C. Niu, *Appl. Catal., A*, 2016, **522**, 54-69.
2. S. Du, S. Wang, Y. Guo, X. Lu, W. Tang, Y. Ding, X. Mao and P.-X. Gao, *Appl. Catal., B*, 2018, **236**, 348-358.
3. S. Amanatidis, L. Ntziachristos, B. Giechaskiel, A. Bergmann and Z. Samaras, *Environ. Sci. Technol.*, 2014, **48**, 11527-11534.
4. Y. Li, S. Cai, P. Wang, T. Yan, J. Zhang and D. Zhang, *Environ. Sci. Technol.*, 2021, **55**, 9276-9284.
5. K. Skalska, J. S. Miller and S. Ledakowicz, *Sci. Total Environ.*, 2010, **408**, 3976-3989.
6. Z. Lei, C. Wen and B. Chen, *Environ. Sci. Technol.*, 2011, **45**, 3437-3444.
7. K. Lehtoranta, H. Vesala, P. Koponen and S. Korhonen, *Environ. Sci. Technol.*, 2015, **49**, 4735-4741.
8. D. K. Pappas, T. Boningari, P. Boolchand and P. G. Smirniotis, *J. Catal.*, 2016, **334**, 1-13.
9. S. Dissanayake, N. Vora, L. Achola, Y. Dang, J. He, Z. Tobin, X. Lu, A. Mirich, P.-X. Gao and S. L. Suib, *Appl. Catal., B*, 2021, **282**, 119573.
10. X. Hu, J. Chen, W. Qu, R. Liu, D. Xu, Z. Ma and X. Tang, *Environ. Sci. Technol.*, 2021, **55**, 5435-5441.
11. P. Zhang, P. Wang, A. Chen, L. Han, T. Yan, J. Zhang and D. Zhang, *Environ. Sci. Technol.*, 2021, **55**, 11970-11978.
12. N. Zhu, Y. Shan, W. Shan, Z. Lian, J. Du and H. He, *Environ. Sci. Technol.*, 2021, **55**, 16175–16183.
13. B. Thirupathi and P. G. Smirniotis, *Appl. Catal., B*, 2011, **110**, 195-206.
14. B. Thirupathi and P. G. Smirniotis, *J. Catal.*, 2012, **288**, 74-83.
15. T. Boningari, P. R. Ettireddy, A. Somogyvari, Y. Liu, A. Vorontsov, C. A. McDonald and P. G. Smirniotis, *J. Catal.*, 2015, **325**, 145-155.
16. T. Boningari, D. K. Pappas and P. G. Smirniotis, *J. Catal.*, 2018, **365**, 320-333.
17. C. Zhu, D. P. Gamliel, J. A. Valla and G. M. Bollas, *Appl. Catal., B*, 2021, **284**, 119719.
18. X. Lu, W. Tang, M. Li, Y. Dang, N. Campbell, Z. Li, S. L. Suib and P.-X. Gao, *Chem. Eng. J.*, 2021, **405**, 126906.
19. L. Zhang, L. Li, Y. Cao, X. Yao, C. Ge, F. Gao, Y. Deng, C. Tang and L. Dong, *Appl. Catal., B*, 2015, **165**, 589-598.
20. X. Lu, M. Li, S. Hoang, S. L. Suib and P.-X. Gao, *Catal. Today*, 2021, **360**, 275-283.
21. X. Lu, W. Tang and P.-X. Gao, *Microsc. Microanal.*, 2018, **24**, 1642-1643.
22. D. V. Bavykin, J. M. Friedrich and F. C. Walsh, *Adv. Mater.*, 2006, **18**, 2807-2824.
23. K. Kordás, M. Mohl, Z. Kónya and Á. Kukovecz, *Transl. Mater. Res.*, 2015, **2**, 015003.

24. Á. Kukovecz, K. Kordás, J. Kiss and Z. Kónya, *Surf. Sci. Rep.*, 2016, **71**, 473-546.
25. N. Sutradhar, A. Sinhamahapatra, S. K. Pahari, H. C. Bajaj and A. B. Panda, *Chem. Commun.*, 2011, **47**, 7731-7733.
26. X. Lu, W. Tang, S. Du, L. Wen, J. Weng, Y. Ding, W. S. Willis, S. L. Suib and P.-X. Gao, *ACS Appl. Mater. Interfaces*, 2019, **11**, 21515-21525.
27. X. Lu, F. Liu, Y. Dang, M. Li, M. Ruan, M. Wu, C. Zhu, T. Mani, S. L. Suib and P.-X. Gao, *Appl. Surf. Sci.*, 2022, **591**, 153116.
28. W. Tang, X. Lu, F. Liu, S. Du, J. Weng, S. Hoang, S. Wang, C.-Y. Nam and P.-X. Gao, *Appl. Catal., B*, 2019, **245**, 623-634.
29. J. L. Williams, *Catal. Today*, 2001, **69**, 3-9.
30. S. Du, W. Tang, X. Lu, S. Wang, Y. Guo and P. X. Gao, *Adv. Mater. Interfaces*, 2018, **5**, 1700730.
31. S. Hoang, X. Lu, W. Tang, S. Wang, S. Du, C.-Y. Nam, Y. Ding, R. D. Vinluan, J. Zheng and P.-X. Gao, *Catal. Today*, 2019, **320**, 2-10.
32. J. Weng, X. Lu and P.-X. Gao, *Catalysts*, 2017, **7**, 253.
33. X. Lu, S. Hoang, W. Tang, S. Du, S. Wang, F. Liu, W. Zhong, S. L. Suib, G. Yang, F.-Y. Zhang and P.-X. Gao, *ACS Appl. Mater. Interfaces*, 2018, **10**, 35164-35174.
34. C. Zhu and G. M. Bollas, *Appl. Catal., B*, 2018, **235**, 92-102.
35. S. Hoang, Y. Guo, A. J. Binder, W. Tang, S. Wang, J. Liu, H. Tran, X. Lu, Y. Wang, Y. Ding, E. A. Kyriakidou, J. Yang, T. J. Toops, T. R. Pauly, R. Ramprasad and P.-X. Gao, *Nat. Commun.*, 2020, **11**, 1062.
36. G. Leofanti, M. Padovan, G. Tozzola and B. Venturelli, *Catal. Today*, 1998, **41**, 207-219.
37. Q. Shi, T. Liu, Q. Li, Y. Xin, X. Lu, W. Tang, Z. Zhang, P.-X. Gao and J. A. Anderson, *Appl. Catal., B*, 2019, **246**, 312-321.
38. P. Suktha, N. Phattharasupakun, P. Dittanet and M. Sawangphruk, *RSC Adv.*, 2017, **7**, 9958-9963.
39. D. A. Peña, B. S. Uphade and P. G. Smirniotis, *J. Catal.*, 2004, **221**, 421-431.
40. H. Chen, Y. Xia, H. Huang, Y. Gan, X. Tao, C. Liang, J. Luo, R. Fang, J. Zhang, W. Zhang and X. Liu, *Chem. Eng. J.*, 2017, **330**, 1195-1202.
41. Z. Fan, J.-W. Shi, C. Gao, G. Gao, B. Wang, Y. Wang, C. He and C. Niu, *Chem. Eng. J.*, 2018, **348**, 820-830.
42. J. He, S.-Y. Chen, W. Tang, Y. Dang, P. Kerns, R. Miao, B. Dutta, P.-X. Gao and S. L. Suib, *Appl. Catal., B*, 2019, **255**, 117766.
43. W. Tang, S. Wang, W. Xiao, S. Du, X. Lu, S. Hoang, J. Ding and P.-X. Gao, *Catal. Today*, 2019, **320**, 196-203.
44. H. Xu, Z. Zhang, J. Liu, C.-L. Do-Thanh, H. Chen, S. Xu, Q. Lin, Y. Jiao, J. Wang, Y. Wang, Y. Chen and S. Dai, *Nat. Commun.*, 2020, **11**, 3908.
45. Y. Zhao, H. Wang, J. Han, X. Zhu, D. Mei and Q. Ge, *ACS Catal.*, 2019, **9**, 3187-3197.
46. Z. Wu, Z. Sheng, Y. Liu, H. Wang and J. Mo, *J. Hazard. Mater.*, 2011, **185**, 1053-1058.
47. T. Gu, Y. Liu, X. Weng, H. Wang and Z. Wu, *Catal. Commun.*, 2010, **12**, 310-313.
48. M. Kang, E. D. Park, J. M. Kim and J. E. Yie, *Appl. Catal., A*, 2007, **327**, 261-269.
49. J. Liu, X. Li, Q. Zhao, J. Ke, H. Xiao, X. Lv, S. Liu, M. Tadé and S. Wang, *Appl. Catal., B*, 2017, **200**, 297-308.
50. D. Yuan, X. Li, Q. Zhao, J. Zhao, S. Liu and M. Tadé, *Appl. Catal., A*, 2013, **451**, 176-183.
51. H. Hu, S. Cai, H. Li, L. Huang, L. Shi and D. Zhang, *J. Phys. Chem. C*, 2015, **119**, 22924-22933.
52. H. Wang, Z. Qu, H. Xie, N. Maeda, L. Miao and Z. Wang, *J. Catal.*, 2016, **338**, 56-67.
53. L. Zhang, L. Shi, L. Huang, J. Zhang, R. Gao and D. Zhang, *ACS Catal.*, 2014, **4**, 1753-1763.
54. Z. Liu, Y. Yi, J. Li, S. I. Woo, B. Wang, X. Cao and Z. Li, *Chem. Commun.*, 2013, **49**, 7726-7728.
55. H. Jiang, L. Zhang, J. Zhao, Y. Li and M. Zhang, *J. Mater. Res.*, 2016, **31**, 702-712.
56. L. Xu, X.-S. Li, M. Crocker, Z.-S. Zhang, A.-M. Zhu and C. Shi, *J. Mol. Catal. A Chem.*, 2013, **378**, 82-90.
57. P. R. Ettireddy, N. Ettireddy, T. Boningari, R. Pardemann and P. G. Smirniotis, *J. Catal.*, 2012, **292**, 53-63.
58. R. Jin, Y. Liu, Y. Wang, W. Cen, Z. Wu, H. Wang and X. Weng, *Appl. Catal., B*, 2014, **148-149**, 582-588.
59. E. Kikuchi and K. Yogo, *Catal. Today*, 1994, **22**, 73-86.
60. F. Yan, Y. Wang, J. Zhang, Z. Lin, J. Zheng and F. Huang, *ChemSusChem*, 2014, **7**, 101-104.
61. D. Meng, W. Zhan, Y. Guo, Y. Guo, L. Wang and G. Lu, *ACS Catal.*, 2015, **5**, 5973-5983.
62. Y. Peng, K. Li and J. Li, *Appl. Catal., B*, 2013, **140-141**, 483-492.
63. L. Zhang, J. Pierce, V. L. Leung, D. Wang and W. S. Epling, *J. Phys. Chem. C*, 2013, **117**, 8282-8289.
64. Y. Peng, C. Wang and J. Li, *Appl. Catal., B*, 2014, **144**, 538-546.
65. B. Liu, J. Liu, S. Ma, Z. Zhao, Y. Chen, X.-Q. Gong, W. Song, A. Duan and G. Jiang, *J. Phys. Chem. C*, 2016, **120**, 2271-2283.